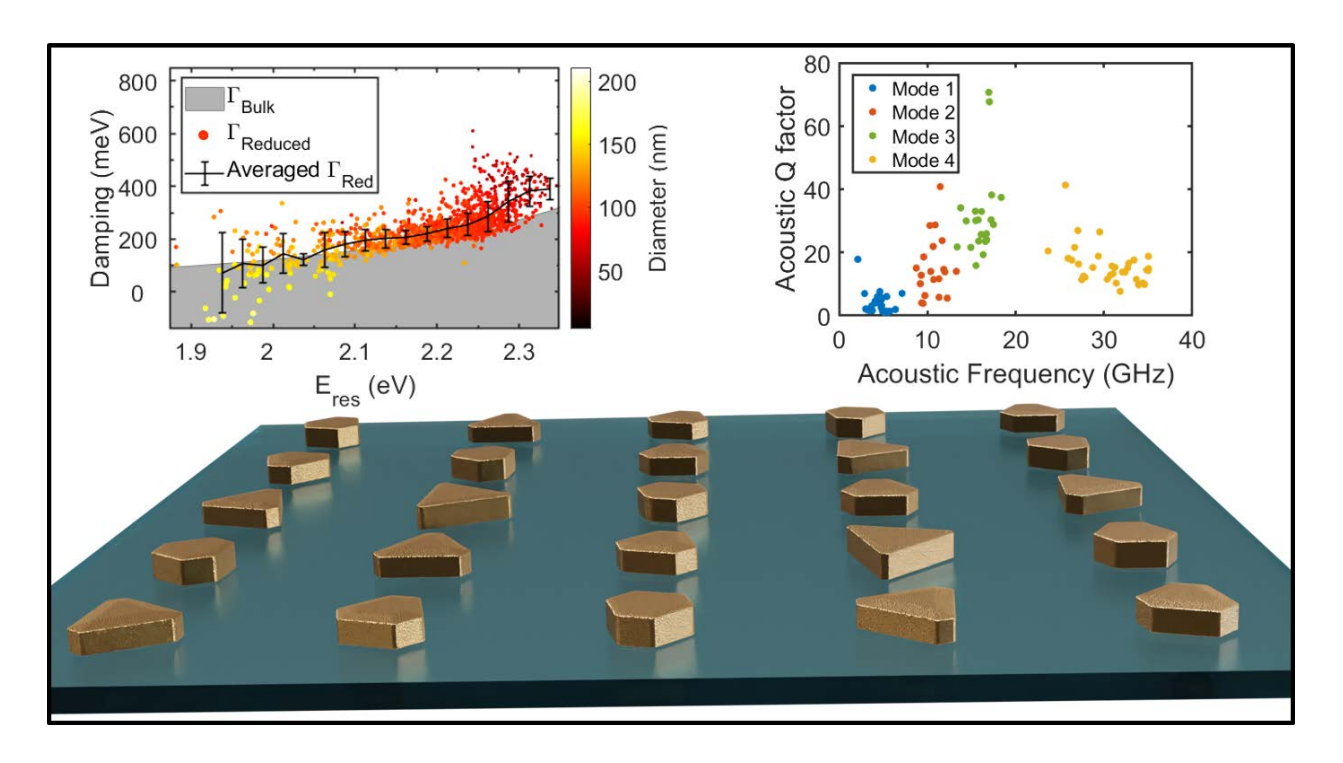
High-Throughput Screening of Optical Properties of Glass-Supported Plasmonic Nanoparticles Fabricated by Polymer-Pen Lithography

Niklas Gross¹, William Wang¹, Sadie Brasel², Emily K. Searles¹, Briley Bourgeois³, Jennifer A. Dionne³, Christy F. Landes^{1,2,4}, Stephan Link^{1,2,*}

Keywords: Single-particle spectroscopy, Surface plasmon, Plasmon dephasing, Acoustic vibrations, Scanning probe block-copolymer lithography

TOC Graphic



¹Department of Chemistry, Rice University, Houston, TX 77005, United States

²Department of Electrical & Computer Engineering, Rice University, Houston, TX 77005, United States

³Department of Materials Science & Engineering, Stanford University, Stanford, CA 94305, United States

⁴Department of Chemical & Biomolecular Engineering, Rice University, Houston, TX 77005, United States

^{*}To whom correspondence should be addressed: slink@rice.edu

Abstract

Optical applications of plasmonic nanoparticles depend critically on particle properties such as relative proximity, composition, crystallinity, and shape. The most common nanoparticle fabrication techniques, colloidal synthesis and electron beam lithography, allow the tailoring of some of these parameters, yet do not provide control over all of them. Scanning probe block-copolymer lithography (SPBCL), a technique that grows nanoparticles on substrates from precisely deposited precursor droplets, merges the advantages of colloidal synthesis and electron beam lithography, and offers high-throughput, precise particle positioning, and composition control. A few challenges with the SBCL method remain: fabrication of optically relevant particle sizes on optically transparent supports, and detailed correlation of their optical and morphological properties. Here, we adapt SPBCL to fabricate large arrays of gold nanoparticles on glass supports. The resulting nanoparticles have varying shapes, and at ~ 100 nm in diameter, they support strong plasmon resonances. In order to fully exploit the high-throughput fabrication method, we designed an automated dark-field microscope and correlated the optical behavior to the mechanical properties as determined through electron and pump-probe microscopy. We find that the SPBCL-synthesized nanoparticles are highly crystalline, supporting both plasmon oscillations and mechanical vibrations with lifetimes comparable to colloidal nanospheres. Our work highlights SPBCL as a promising and versatile synthesis approach for plasmonic nanoparticles, leading the way toward extensive screening capabilities for optical properties and hence improved potential applications.

Introduction

The design of efficient optical applications based on plasmonic nanoparticles demands excellent control of particle shape and positioning as well as the ability to produce particles of high crystallinity.¹⁻⁴ Additionally, the commercial utilization of plasmonic nanoparticles requires their availability en masse and at low cost. Both physical particle properties as well as affordability are determined by the particle fabrication, and various fabrication techniques have been developed to meet the aforementioned demands.⁵⁻⁹ Among the most commonly employed nanoparticle fabrication techniques are chemical particle growth (colloidal synthesis) and electron beam lithography (EBL),^{10, 11} which have been used to fabricate plasmonic nanoparticles for applications in sensing, medicine, catalysis, and photovoltaics.¹²⁻¹⁶

However, neither colloidal synthesis nor EBL offer full control over the physical particle properties while maintaining affordability to fabricate particles with high-throughput. Colloidal synthesis grants access to a wide range of particle shapes with typically highly crystalline structures, but lacks the ability to arrange nanoparticles in defined positions, which has led to much interest in the self-assembly of these particles.^{17, 18} On the other hand, EBL allows the fabrication of nanoparticles with arbitrary shapes at precisely controlled positions, but leads to polycrystalline nanostructures with lower optical and mechanical quality (Q) factors compared to colloidal nanoparticles.¹⁹⁻²¹ While colloidal synthesis is more affordable and can produce nanoparticles in bulk, EBL is more expensive and has lower throughput because it requires the use of electron beam irradiation to pattern individual particle shapes. These fabrication tradeoffs lead to a lack in methods that allow one to both affordably produce highly crystalline nanoparticles with high-throughput while also enabling control of particle size and position. Other techniques have been developed to address this issue but each face limitations in terms of size and position control.²²⁻²⁹

Polymer-pen-lithography (PPL) represents a fusion of colloidal synthesis and EBL and has the potential to fill the gap in the nanoparticle fabrication library. Scanning probe block-copolymer lithography (SPBCL), a technique based on PPL, uses polymer pyramids as pens to deposit small droplets of metal precursor solutions onto substrates. These droplets are subsequently grown into nanoparticles through a thermal annealing procedure. The utilization of large arrays that contain thousands of pens allows SPBCL to apply different metal precursors at the same time or employ precursor mixtures for multi-component particles. With these advantages, SPBCL has been used to fabricate extensive nanoparticle libraries with multi-metallic particles containing up to five different metals, forming alloys or separate metal phases, depending on their miscibility. However, so far, studies have focused on smaller nanoparticles, predominantly for applications in catalysis, with diameters not exceeding ~60 nm. Addition, mostly conductive and non-transparent substrates or thin membranes that are ideal for electron microscopy have been utilized, also because of their low surface roughness. Addition has the potential procedure and procedure and the procedure and procedure and the procedure and p

substrates are either incompatible or disadvantageous for optical studies, while small nanoparticles do not scatter efficiently enough to be observed by single-particle spectroscopy so that effects of sample inhomogeneities can be deciphered. Consequently, there is a need to extend SPBCL to fabricate larger metal nanoparticles with significant optical scattering cross sections on transparent substrates for the detailed analysis of their optical properties.

Here, we used SPBCL to fabricate gold nanoparticles (AuNPs) with diameters ranging from 50 to 200 nm on glass substrates and characterized their optical and mechanical properties. We employed dark-field scattering spectroscopy to investigate their plasmonic properties and in particular determined plasmon damping to understand the quality of the resonance in comparison to colloidal AuNPs of similar diameter. The dimensions of the SPBCL AuNPs were obtained by scanning electron microscopy (SEM) to yield the diameter and atomic force microscopy (AFM) to give the thickness, while transmission electron microscopy (TEM) revealed their crystalline nature. We further characterized the AuNP shapes through Wulff construction theory and evaluated the computed shapes using the agreement of their simulated optical spectra based on discrete dipole approximation (DDA) simulations with experimental data. Lastly, we employed ultrafast transient transmission microscopy to study the acoustic vibrations of SPBCL AuNPs. The experimentally obtained acoustic frequencies were compared to simulations based on the finite element method (FEM) to assign the observed acoustic modes. Our results demonstrate plasmon lifetimes and acoustic Q factors that are comparable to those of colloidal gold nanospheres (AuNSs) and larger than those of comparable AuNPs fabricated using EBL, confirming that SPBCL produces highly crystalline AuNPs with promising optical applications.

Methods

Scanning Probe Block Copolymer Lithography

Gold nanoparticles (AuNPs) were synthesized through SPBCL, a method based on polymer pen lithography. 31,37 Polymer pen arrays of ~500 x 500 polydimethylsiloxane pyramids with inter-pen distances of 100 µm were purchased from TERA-print. The block-copolymer poly(2-vinyl pyridine)-b-poly(ethylene oxide) with molecular weight of M_n (x10³) = 1.5-b-2.8 g/mol was purchased from Polymer Source. The precursor Au (III) chloride trihydrate (HAuCl₄ · 3 H₂O) was purchased from Sigma Aldrich. Millipore water was used to make precursor solutions with concentrations of 14.1 mg/ml. Similarly, polymer solutions with a concentration of 5 mg/ml were made. Au and polymer solutions were combined in a ratio of approximately 1:4 to generate a combined solution, referred to as ink, with a ratio of 1:2 between Au ions and pyridine groups. The ink was stirred overnight for at least 8 hours to allow for the association of metal ions with the 2-vinyl pyridine groups and formation of nanoscale micelles due to the low water solubility of the pyridine groups. 31 The more water soluble ethylene oxide groups then

facilitated the ink transfer.³¹ Before usage, the polymer pen array was cleaned in oxygen plasma (Harrick Plasma, PDC-32G) for two minutes on medium, and a volume of 0.25 ml ink was spincoated (Laurell, WS-650MZ-23NPPB) onto the array with rates of 250 rpm (30 seconds) and 2500 rpm (1 minute) before leaving it to dry for 15 minutes. For the substrates, glass coverslips were cleaned in Millipore water, a solution of Liquinox soap, acetone, isopropanol, and again Millipore water under sonication for 10 minutes each and dried under a nitrogen stream. Using a home-built mask, a Au frame was then evaporated onto the glass substrates (Corning, CB-0102, alkaline earth boro-aluminosilicate) to enable substrate alignment before ink deposition. The substrates were then stored for at least 8 hours in a desiccator with a vial containing a 1:3 mixture of hexamethyldisilazane (HMDS) and hexane to make the surface hydrophobic. A commercial M-series Teraprint instrument was used to deposit small droplets of the ink via the pyramids on the prepared substrates. After initial alignment, the pen array was incubated for 60 minutes under 90% humidity. Arrays of 10x10 ink droplets with distances of 5 μm were accomplished by bringing polymer pens and substrate into contact in a manually defined pattern. At each contact we applied a force of ~1500 mN for a contact time of 5 s with approach and retract velocities of 100 and 150 µm/s, respectively. Following deposition, these substrates were then annealed in a tube furnace (Thermcraft, XST-3-0-24-3V2-F01-C-D-H-P) under nitrogen atmosphere at 150° C for 12 hours, above the glass transition temperature of the employed polymer to allow for metal ion diffusion and aggregation. Subsequently, the temperature was raised to 500° C for 4 hours to decompose the polymer and reduce the metal ions before cooling down to room temperature.³⁷ The ramping time between each step was 1 hour. SEM images of fabricated nanoparticles initially indicated carbon residues, which were however easily removed using oxygen plasma (Harrick-Plasma PDC-32G, 1 min, medium) or under irradiation with ultrafast laser pulses $(4.75 \times 10^4 \text{ to } 1.59 \times 10^4 \text{ W/cm}^2)$. Commercial gold nanospheres (AuNSs) were purchased from nanoComposix with diameters of 50 nm, 70 nm, 80 nm, and 100 nm according to the manufacturer.

Single-Particle Scattering Spectroscopy

Single-particle scattering spectra were measured in a dark-field geometry using a Zeiss microscope (Axio Observer.D1). Light from a halogen lamp (Zeiss, HAL 100) was focused onto the sample using an oil-immersion condenser (Zeiss, achromatic-aplanatic NA 1.4) in dark-field mode. The scattered light was collected through a refractive air objective (Zeiss, EC Epiplan-NEOFLUAR, 50x, NA 0.8) and directed through a slit towards a spectrometer (Andor Shamrock) that was equipped with a charge-coupled device (CCD) camera (Andor, iDus DU420A-BEX2-DD). Initial dark-field scattering images were taken to identify single AuNP locations by switching the grating to its zero-order diffraction mode and fully opening the slit in front of the spectrometer. The slit was then set to 150 µm to limit the light that reached the camera and a piezo scanning stage was used to move identified AuNPs into the slit aperture to record

single-particle spectra with the grating set to the first-order diffraction at a center wavelength of 600 nm. The employed grating had a groove density of 300 grooves per millimeter and a blaze wavelength of 500 nm. To take advantage of the large and ordered AuNP arrays obtained through SPBCL, we automated the measurement process using LabVIEW and our single-particle tracking algorithm TROIKA.³⁸ In this process we identified and labeled large numbers of AuNP positions at once, and systematically measured single-particle spectra using the piezo stage in a stepwise scanning procedure. Additionally, we accounted for drift due to the prolonged measurement times. In this drift correction step, we employed the piezo stage to scan the area around each AuNP position in XY and subsequently Z to determine the location of largest total scattering intensity. We chose a total of 16 scanning steps for each AuNP at an exposure time of 0.2 seconds and then measured the drift-corrected spectrum with an exposure time of 2 seconds. This procedure allowed us to measure 100 drift-corrected single-particle spectra in approximately 20 minutes. No change in the optical properties was observed before and after the removal of carbon residue.

Single-Particle Ultrafast Transient Transmission Microscopy

Transient transmission microscopy was performed using a homebuilt setup that combined an ultrafast pump-probe scheme with a single-particle microscope (Zeiss, Axio Observer.D1m). The light source was a Ti:Sapphire oscillator (KMLabs, Griffin-10) that was pumped by a 532 nm laser (Coherent, Verdi G10) and produced sub-100 fs light pulses at a frequency of 86 MHz and a center wavelength of 800 nm. The average output power of the oscillator was 1.05 W, of which ~25% was used for the pump beams, either at the fundamental of the oscillator or at 400 nm after second harmonic generation in a beta barium borate crystal (Altos, BBO-1004H). Another ~25% of the laser output were directed into a nonlinear photonic crystal fiber (NKT Photonics, FemtoWHITE 800) to generate a white light continuum with a wavelength range of 500-1000 nm for the probe. From the continuum, spectral slices of 25 nm were selected with bandpass filters. In this study, 400 nm was used as the pump to excite Au interband transitions. We utilized a probe wavelength of 800 nm because as the fundamental oscillator output it granted optimum power stability. An optical delay stage (Newport, UTS150CC) in the probe beam path controlled the temporal overlap of the pump and probe pulses, and the pump was modulated with an optical chopper (Newport, Model 3502) at 8 kHz. A dichroic mirror recombined pump and probe beams and an oil immersion objective (Zeiss, Plan-Apochromat, 63x, 1.4 NA) focused the beams on the sample. The light was collected by a receiving objective (Zeiss, LD Achroplan, 40x, 0.6 NA) in a transmission geometry. The energy densities of the pump and probe beams at the sample were approximately $4.75 \times$ 10^4 and 1.59×10^4 W/cm² with beam sizes of 500 and 600 nm, respectively. Optical filters were subsequently utilized to remove the pump beam, while the probe beam was detected by a photodiode (Femto, DHPCA-100-F). The detected transmitted signal T was directed to a lock-in amplifier (EG&G Instruments, Model 5302) that was referenced to the pump modulation frequency to read out changes in

the pump-induced transmitted signal ΔT . ΔT was digitized with a data acquisition board (National Instruments, USB-6229) and collected with a custom LabVIEW program. Using an oscilloscope (Tektronix TDS 2024C) to determine T from the photodiode, the differential transient transmission $\Delta T/T$ was obtained. Transient transmission images were acquired by focusing the spatially and temporally overlapped pump and probe beams onto the sample, which was raster-scanned with a piezo stage (Physik Instrumente, P-517.3CL). Time transients of $\Delta T/T$ were measured by positioning a single AuNP in the focus of the overlapped beams and changing pump-probe delay times. All transients were repeated at least two times and averaged to increase the signal-to-noise ratio, to confirm the setup stability, and to exclude thermal reshaping of the AuNPs due to laser heating. Because the employed laser pulses removed any carbon residue, its effect on the acoustic properties of nanoparticles was eliminated in these measurements.

Wulff Construction

AuNP shapes were generated through the published Wulff construction software WulffDDSCAT.³⁹ The experimentally observed hexagonal and truncated triangular AuNPs were reproduced using the AuNP diameters from electron microscopy images and under the assumption of a twin plane. The applied settings for each case are summarized in Table S1. The chosen parameters were adapted and modified from previous literature, where instructions and definitions of each parameter are provided.³⁹

Discrete Dipole Approximation (DDA) Simulations

Using the above-mentioned Wulff construction software WulffDDSCAT, the generated AuNP shapes were translated into arrays of dipoles. For all simulations, inter-dipole distances were chosen so that shapes were comprised of more than 200,000 dipoles. The free DDA software DDSCAT was employed to calculate scattering spectra with a spectral range from 400 to 900 nm. ⁴⁰ Assuming that each AuNP laid flat on the substrate, we used the generated shapes to approximate the fraction of total surface area that was in contact with the substrate. This way, we determined an effective refractive index of 1.1 corresponding to a refractive index between air (refractive index = 1) and glass (refractive index = 1.5). ⁴¹ The AuNP was illuminated with light that travelled perpendicularly to the horizontal AuNP plane to excite the in-plane plasmon resonance. The simulation was repeated light with polarization shifted by 90°. Averaging these orthogonal polarizations was used to mimic the unpolarized light in the experiment.

Finite Element Method (FEM) Simulations

The structural mechanics module of the commercial software COMSOL was used to simulate the acoustic vibrations of SPBCL AuNPs. The free 3D visualization software Blender was utilized to approximate the AuNP shapes that were generated through Wulff construction, and the resulting images were imported into COMSOL. Because of the absence of adhesion layers between AuNPs and substrate, we considered the substrate to have minimum effect on the acoustic modes of the AuNPs apart from

being a damping source, corresponding to the weak binding regime. 42 We thus performed simulations for the limiting case of free AuNPs without a substrate. 43 Note that no Q factors were calculated in this case, because energy loss into the environment was ignored and FEM does not consider intrinsic damping sources such as defects. Acoustic vibrations were simulated by calculating the AuNP response to uniform pressure at all boundaries, recreating the uniform heating of a single AuNP in the experiment. A frequency domain study was performed to obtain the acoustic response to uniform pressures applied with frequencies between 0 and 50 GHz. Efficiently excited acoustic modes were then identified through maxima in the stored acoustic energy spectra. The experiment probed acoustic modes through changes in the in-plane plasmon resonance. We therefore followed examples in the literature, and calculated the change in AuNP dimension by integrating the displacement in order to determine modes that lead to the largest changes in the plasmon resonance and are likely to be observed experimentally. By correlating efficiently excited modes with efficiently probed modes, we identified acoustic vibrations that were most probably observed in the experiment. The 'Extra fine' mesh settings were applied so that the mesh size was not larger than one tenth of the AuNP thickness.²⁰ It is important to note that the acoustic frequencies and mode profiles are extremely sensitive to changes in particle shape and dimension, ²⁰ as directly evident from the different simulated profiles for the structurally comparable truncated triangular and hexagonal AuNPs. We chose truncated triangular and hexagonal morphologies in our simulations due to their high abundance in our samples, and because we analyzed them by Wulff construction theory too (Figure 2b). However, not all AuNPs included in Figure 4b were of truncated triangular or hexagonal shape, as illustrated in Figure S13. Discrepancies in simulated and experimental frequencies were therefore likely due to shape differences.

Scanning Electron Microscopy (SEM)

AuNP images were taken on A FEI Quanta 400 ESEM FEG. Due to the nonconductive nature of glass substrates, all images were measured under environmental conditions in a water atmosphere at \sim 4x10⁻⁴ Torr. Images were recorded with a dwell time of 10 μ s and a voltage of 15 kV. SEM images were used to determine AuNP diameters through the software ImageJ, defined as the average of the maximum and minimum Feret.

Transmission Electron Microscopy (TEM)

TEM micrographs were taken on a JEOL 2100 Field Emission Gun TEM. AuNPs were sonicated off the transparent supports and transferred to TEM grids (Electron Microscopy Sciences, 300 copper mesh) to allow high-resolution micrographs to be captured. The diffraction pattern in the inset of Figure 2d was obtained through fast Fourier transform (FFT) of the image shown in Figure 2d. The diffraction patters in the insets of Figures 2e and 2f were acquired similarly from the crystalline regions above and below the twin plane.

Atomic Force Microscopy (AFM)

AFM images were recorded on a Park AFM NX20 microscope. Images were taken in tapping mode with commercially fabricated cantilevers (NCHR-10 Nano World). AFM images were analyzed with XEI software to extract AuNP thicknesses as displayed in Figure S8.

Plasmonic Damping Calculations

We consider the plasmon damping as $\Gamma_{Total} = \Gamma_{Bulk} + \Gamma_{Rad} + \Gamma_{Surf} + \Gamma_{CID}$ with bulk damping Γ_{Bulk} , radiation damping Γ_{Rad} , electron-surface scattering Γ_{Surf} , and chemical interface damping Γ_{CID} . ^{44, 45} Bulk damping Γ_{Bulk} includes the Drude resistance γ_b as well as interband damping Γ_{IB} . The Drude resistance γ_b = 73 meV describes electron scattering off other electrons, ⁴⁶ defects, or phonons, while interband contributions account for plasmon decay into interband transitions, which have a threshold of 1.7-1.8 eV for Au. 45, 47 Bulk damping is governed by the metal itself and is obtained from its frequency-dependent dielectric function. Here, we used values for the dielectric function reported by Olmon et al. 48 Γ_{CID} represents a loss mechanism due to modifications at the AuNP interfaces. For SPBCL AuNPs, we assume Γ_{CID} to be negligibly small as the final annealing temperature at 500°C in the fabrication procedure is larger than the decomposition temperature of the utilized polymer (409°C), likely leading to the full decomposition of any organic material.³⁷ Γ_{Rad} considers the loss of energy through light radiation and increases with the AuNP volume according to $\Gamma_{Rad} = h\kappa V/\pi$. We used a radiation damping constant $\kappa =$ 3.34 x 10⁻⁷ fs⁻¹ nm⁻³, ⁴⁹ while the volume V of each individual AuNP was determined by multiplying its area, as obtained via the average diameter extracted from correlated SEM image, with its calculated maximum thicknesses according to the results in Figure 1d and considering a thickness correction factor of 0.75 described in Figure S8. Γ_{Surf} defines damping due to electron-surface scattering and is calculated as $\Gamma_{\text{surf}} = A_{\text{Surf}} v_F / L_{\text{eff}}$. Here, $v_F = 1.4$ nm fs⁻¹ is the Fermi velocity, ⁵⁰ Leff is the effective mean free path of electrons in the AuNPs, and A is a surface scattering parameter. Because we assume the SPBCL AuNPs to be free of ligands as discussed above, we utilized a value of $A_{Surf} = 0.12$, as previously reported for bare Au nanorods in ethanol.⁴⁴ While several expressions for Leff have been reported,⁵¹ we found good agreement when using the relationship L_{eff} = 2H which was derived for thin cylindrical particle geometries with thickness H. The thickness correction factor was applied for this calculation of Leff as well. The thin cylindrical geometry is most similar to our AuNPs with thicknesses considerably less than the respective diameters. However, Figure S9 also illustrates that comparable values for the residual plasmon damping Γ_{Red} were obtained when calculating L_{eff} using the more general expression of L_{eff} = 4V/S with S corresponding to the AuNP surface area.⁵¹

Results and Discussion

SPBCL was employed to fabricate AuNPs on glass substrates (Figure 1a). Aqueous solutions of the block-copolymer, poly(2-vinyl pyridine)-b-poly(ethylene oxide), and the gold (Au) precursor, Au (III) tetrachloride trihydrate (HAuCl₄·3H₂O), were loaded onto polymer pen arrays consisting of ~500 x 500 pens and deposited onto substrates by establishing contact between pens and substrate. A piezo stage was programmed to create arrays of 10 x 10 droplets per pen. The droplets acted as nanoreactors that each produced a single AuNP in a thermal annealing procedure under nitrogen atmosphere.³⁷ Considering a substrate area of about 1.5 cm², approximately 2.25 million AuNPs with controlled positions were generated in each synthesis. Further experimental details are described in the methods section.

The fabricated SPBCL AuNPs were arranged with high spatial precision, and exhibited different shapes across all arrays and samples. Figure 1b on the left displays a cutout of a 3 x 3 AuNP sub-array as an example of the symmetric arrangement within each array. From a total of ~1400 AuNPs from 22 arrays and four different samples, we identified a common prismatic base shape with different levels of truncation and edge roundness. Using SEM images as presented on the right of Figure 1b, and following previously introduced nomenclature, ⁵² we categorized the AuNPs into groups of (I) truncated triangular, (II) hexagonal, and (III) circular shapes, with (IV) an additional group encompassing other derivatives of the prismatic base shape. Truncated triangular AuNPs constituted 43% of all AuNPs, while hexagonal and circular AuNPs represented 27% and 23%, respectively. Only 7% of all AuNPs could not be assigned to these three shapes (Figure S1).

AuNP diameters between 50 and 200 nm were achieved by controlling the deposited ink volume through pen-substrate contact force and time. The diameters were extracted from SEM images through the software ImageJ and defined as the average of the minimum and maximum Feret. Figure 1c demonstrates that small standard deviations down to ±5 nm were achieved. While Figure 1c only highlights the diameter distributions of three individual arrays containing 10 x 10 AuNPs, for completeness and to avoid any bias in our representation, the diameter distributions of all additional measured arrays are presented in Figure S2. Within each sample, we observed variations in the average AuNP diameter between arrays, and ascribe them to dissimilarities in the height of individual pens, leading to differences in the actual applied contact force for each pen. These diameter variations between arrays were also observed by Mirkin and coworkers. Furthermore, for a few arrays, the standard deviation could reach almost 20% of the average diameter, caused by small subpopulations of larger AuNPs (Figure S2, sample 4, purple). We observed that this effect occurred concurrently with instable pen-substrate contact forces during the deposition process, and emphasize the importance of experimental settings to reduce or eliminate large diameter distributions as well as unwanted synthesis products (Figure S3).

SPBCL AuNPs exhibited diameters approximately twice their thickness. In addition to the inplane diameter extracted from the SEM images, AFM was used to determine AuNP thicknesses from randomly chosen arrays on multiple samples. Figure 1d displays linear fits to the dependence of maximum AuNP thicknesses on their corresponding diameters for each sample, all showing a diameter-to-thickness relationship of approximately 2:1, although with slightly varying offsets. To consider uncertainties in both experimental and data analysis steps, we averaged the slopes and calculated the individual AuNP thickness as 0.52x - 19.6 nm, with x being the AuNP diameter. Lastly, we did not observe a dependence of AuNP shape on diameter (Figure S4).

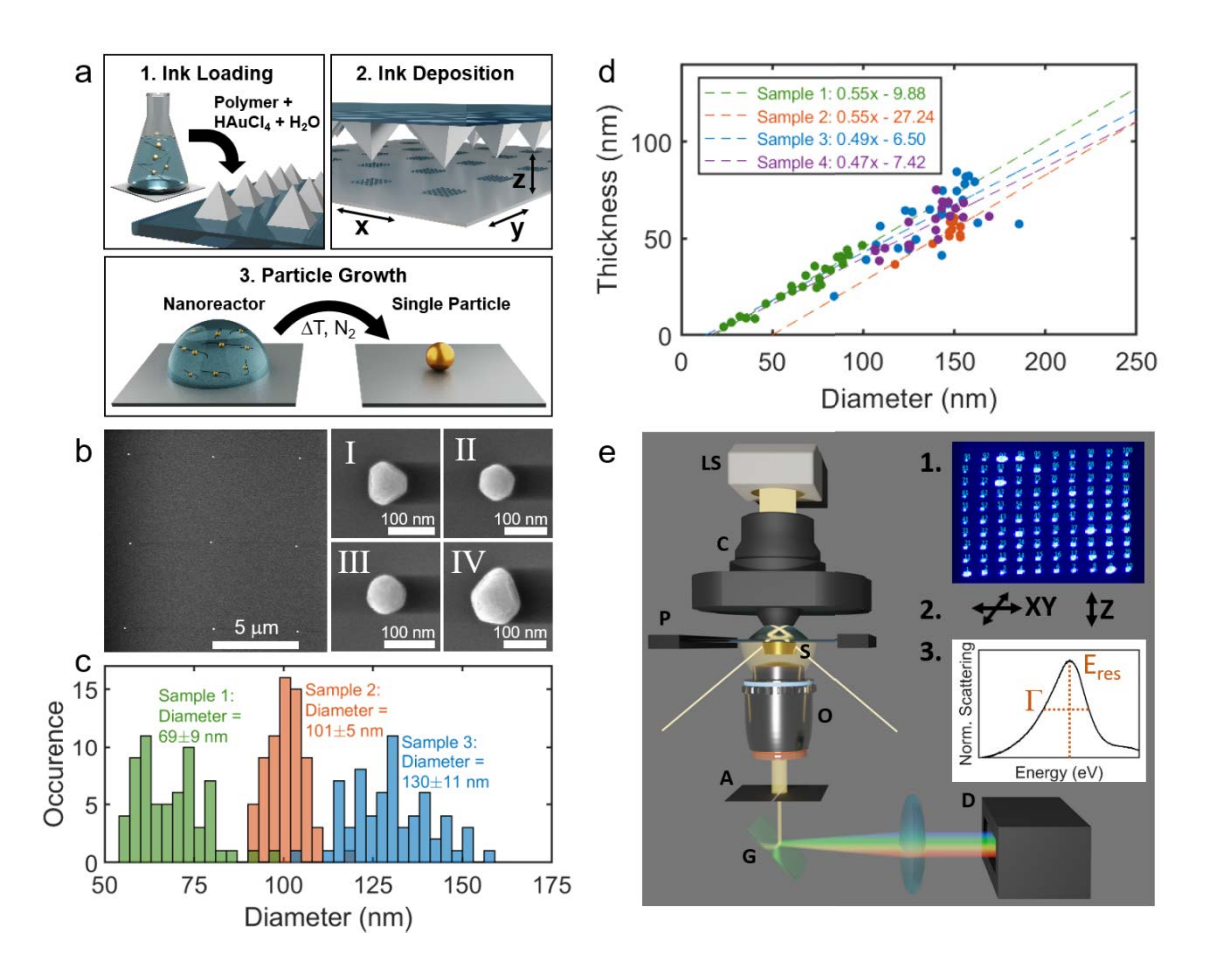


Figure 1: SPBCL-synthesized AuNPs growth and characterization. a) Schematic of the AuNP synthesis with SPBCL. b) Left: Example SEM image of a 3 x 3 cutout of a 10 x 10 AuNP array. Right: Example SEM images of AuNP shape categories: (I) truncated triangular, (II) hexagonal, (III) circular, and (IV) other derivatives of the prismatic base shape. c) Histograms of AuNP diameters for three individual arrays on three different samples. d) AuNP thicknesses plotted against their correlated diameters, with linear fits. e) Schematic and work-flow for automated dark-field microscope. (Step 1)

Initial acquisition of dark-field images and labeling of positions. (Step 2) Drift correction. (Step 3) Acquisition of drift-corrected spectrum and extraction of plasmon energy and damping. LS: Light Source; C: Condenser; P: Piezo Stage; S: Sample; O: Objective; A: Aperture/Slit; G: Grating; D: Detector/CCD camera. The tube lens and focusing lens between objective and aperture were omitted for clarity.

Automated dark-field spectroscopy facilitated the efficient characterization of the optical scattering properties of SPBCL AuNPs (Figure 1e). We took advantage of the symmetric AuNP arrays created by SPBCL, and developed an automated dark-field microscope that enabled us to measure scattering spectra of 100 AuNPs in approximately 20 minutes. In this methodology, initial dark-field images, recorded with the charge-coupled device (CCD) camera while the spectrometer slit was fully open and the grating set to act as a mirror, were used to identify and label all AuNP positions within an array, applying our previously published single-particle tracking algorithm. A piezo stage was then used to sequentially move labeled positions into the field-of-view defined by the now only partially open slit of a spectrometer to measure single-particle spectra. To account for any sample and focus drift during the total measurement time for 100 AuNPs, we implemented a scanning algorithm that corrected for these effects by identifying the maximum scattering intensity in the three-dimensional proximity of each labeled position. This setup, in combination with the high-throughput of SPBCL, enabled us to acquire drift-corrected optical scattering spectra with high throughput and can be readily adapted to record single-particle extinction and photoluminescence spectra as well.

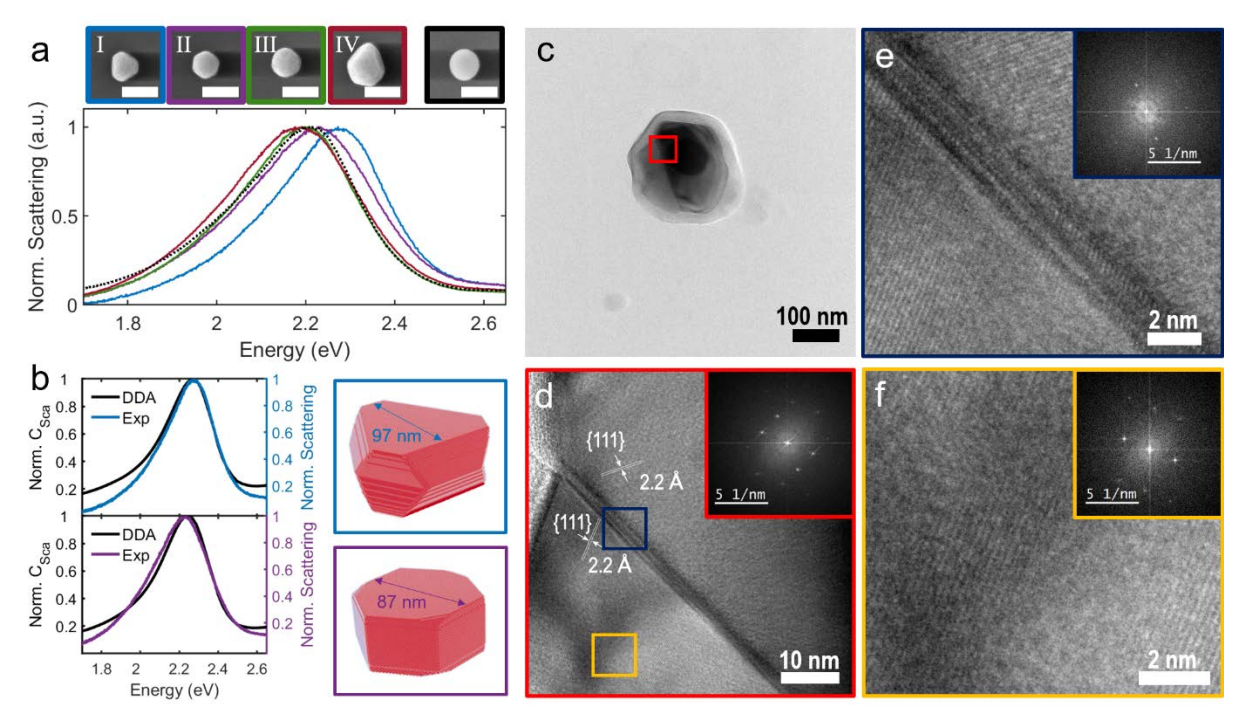


Figure 2. SPBCL-synthesized AuNPs optical and crystalline properties. a) Single-particle scattering spectra of the four AuNPs shown in Figure 1b for each shape category: truncated triangular (I, blue), hexagonal (II, purple), circular (III, green), and other derivatives (IV, red), compared to a colloidally grown AuNS (black, dotted line). Correlated SEM images are shown above the spectra. Scale bars correspond to 100 nm. b) Left: Experimental scattering spectra of the truncated triangular and hexagonal AuNPs presented in a), overlaid with DDA simulated scattering spectra based on AuNP shapes generated through kinetic Wulff construction theory. Right Column: Truncated triangular and hexagonal AuNP shapes generated through kinetic Wulff construction theory. c) TEM image of a single SPBCL AuNP. The red square marks the magnified area displayed in d). The blue and yellow squares again mark magnified areas shown in e) and f), respectively. The images detail high crystallinity even in proximity of the twin plane where the crystal planes meet at an angle of ~130°. f) Zoomed-in high-resolution TEM (HRTEM) image of the yellow square in d), again confirming the high crystallinity of SPBCL AuNPs. Insets in d-f): Diffraction pattern obtained through fast Fourier transform (FFT) of the image shown in d) and the crystalline regions above and below the defect, respectively.

SPBCL AuNPs exhibited scattering spectra that were comparable to those of colloidal AuNSs, indicating high quality plasmon resonances. Figure 2a highlights spectra for truncated triangular (blue), hexagonal (purple), and circular (green) AuNPs, all of which had diameters of approximately 100 nm. We observed asymmetric spectral shapes similar to those of AuNSs,⁵³ leading us to determine plasmon resonance energies and damping directly from the experimental spectra as indicated in the inset of Figure

le, rather than through Lorentzian fits. 45 Overall, we found statistically similar resonance energies (E_{res}) for particles of similar size but different shape (Figure S5). However, slightly larger average E_{res} for hexagonal and circular AuNPs compared to truncated triangles indicated that AuNPs with more rounded edges and increased truncation have larger E_{res}. This observation is in agreement with previous reports that have related larger E_{res} for truncated nanoprisms to more spread out charge distributions. 54-56 Furthermore, when comparing the circular SPBCL AuNP spectrum (green) to the spectrum of a colloidal AuNS with an alike diameter (black, dotted) we found excellent agreement. These AuNSs are known to be highly crystalline, 57 and the similarity in spectra suggests that AuNPs fabricated by SPBCL have high quality plasmon resonances. This conclusion will be further confirmed below on a large dataset of single-particle spectra.

The experimentally observed SPBCL AuNP shapes are the result of kinetic particle growth effects. We made use of Wulff construction theory to further evaluate the structural properties of SPBCL AuNPs. Wulff construction theory comprises two variants, thermodynamic and kinetic, which consider surface free energies or growth velocities to predict particle shapes, respectively.⁵⁸ Here, we applied a kinetic Wulff construction model that included growth enhancement at favorable nucleation sites such as twin boundaries and allowed us to successfully reproduce the experimentally observed AuNP shapes.⁵⁸ Figure 2b (right) shows computed particle shapes resembling the observed truncated triangular and hexagonal AuNPs. These shapes were obtained under the assumption of single-crystallinity with the exception of a single planar twin plane, suggesting similar crystalline features for the SPBCL AuNPs. Indeed, twin planes have been discussed for AuNPs with prismatic shapes comparable to the AuNPs investigated here.⁵² We were not able to reproduce circularly shaped AuNPs or derivatives of the prismatic shape. These shapes are likely the result of additional growth effects that are not included in the here applied kinetic Wulff construction theory.

The utilized block copolymer likely affects the shape of SPBCL AuNPs. Kinetic Wulff construction theory has been employed to describe AuNPs that also exhibited prismatic shapes but were fabricated by colloidal syntheses using polyvinylpyrrolidone (PVP) as surfactant.⁵⁸ Interestingly, PVP has comparable functional groups to the 2-vinylpyridine groups in the block-copolymer utilized here, and the similar prismatic AuNP shapes suggest that the block-copolymer acts like a surfactant in SPBCL. Further control over size and shape of larger plasmonic particles should therefore be possible by varying the pyramid-substrate contact time, contact force, incubation time, and the employed polymer.

Excellent agreement between DDA simulations of scattering spectra using as input the AuNP shapes generated from Wulff construction theory with experimental spectra further validated our shape analysis. As presented in Figure 2b (right), Wulff construction shapes were computed with the measured diameters and calculated thicknesses of the truncated triangular (blue) and hexagonal (purple) SPBCL

AuNPs from Figure 2a. The obtained shapes were then applied in DDA simulations to compare to the corresponding experimental spectra.^{39, 59} The excellent agreement of the simulated with the experimental spectra without any adjustable parameters, displayed in Figure 2b (left), provided additional support for our interpretation of these SPBCL AuNP shapes along with their highly crystalline structure. The DDA simulations also yielded electric field distributions (Figure S6) that confirmed an in-plane plasmon mode as the origin of the observed scattering resonances, as expected for excitation in our experimental setup with unpolarized light emerging from a condenser and incident on the sample at an angle of 67°.

Finally, TEM images directly confirmed the so far inferred crystalline nature of the SPBCL AuNPs. The TEM image of a single SPBCL AuNP in Figure 2c shows multiple regions inside the AuNP and an outer oxide layer, which resulted from the removal of the AuNP off the glass substrate by sonication into aqueous solutions to enable transfer onto a TEM substrate (Figure S7). The highlighted area of the AuNP, magnified in Figure 2d, revealed a twin plane within the AuNP, separating two regions of (111) Au crystal planes as confirmed by the same inter-lattice distance of 2.2 Å. The FFT of the entire image is given in the inset with distinct diffraction spots confirming the high degree of crystallinity. Furthermore, HRTEM images in Figures 2e and 2f clearly show lattice planes, as confirmed by the FFTs in the insets for the crystallites above (blue) and below (yellow) the twin plane. When combined, these FFTs equaled the FFT from the entire image in Figure 2d. The observation of (111) Au crystal planes was indicative of the flat top-side of Au nanoprisms, suggesting that the illustrated AuNP was positioned flat on the support. Therefore, the occurrence of non-horizontally aligned twin planes indicated that additional twin planes can be present within some of the heterogeneous particle shapes. Overall, the presented TEM images established high crystallinity for SPBCL fabricated, large AuNPs with diameters on the order of 100 nm.

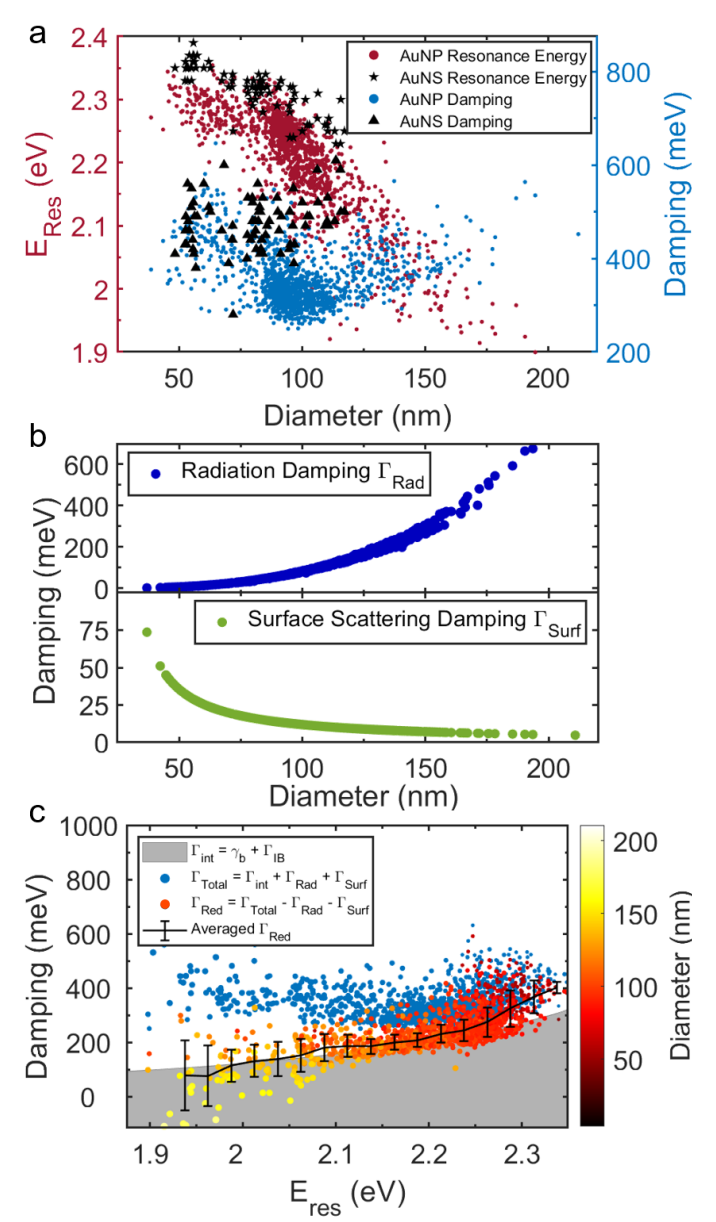


Figure 3. The diameter-dependent plasmon damping for SPBCL-synthesized AuNPs and colloidal AuNSs of comparable diameter and resonance energy E_{res} , related to radiation damping and surface scattering. (a) E_{res} (left, red) and plasmon damping (right, blue) of ~1400 single SPBCL AuNPs as a function of their diameter, compared to values for colloidal AuNSs, given by overlaid black stars and triangles, respectively. (b) Radiation damping (blue) and surface scattering (green) calculated for each SPBCL AuNP with its corresponding diameter and thickness. c) Total measured plasmon damping Γ_{Total} for each SPBCL AuNP (blue) and residual plasmon damping Γ_{Red} after subtraction of radiation damping and surface scattering vs. E_{res} (red to yellow indicating increasing diameter). The black line and error bars represent the binned and averaged values of Γ_{Red} with bin widths of 0.025 eV.

SPBCL AuNPs support plasmon resonances that are of similar or higher quality compared to colloidal AuNSs. The quality of the SPBCL AuNP plasmon resonance was evaluated by analyzing the homogeneous single-particle linewidth, revealing that plasmon damping of SPBCL AuNPs was overall smaller than for colloidal AuNSs of similar diameter and comparable E_{res}. Figure 3a summarizes the resonance energies E_{res} (red) and plasmon damping (blue), as obtained from the linewidth, for ~1400 AuNPs as a function of their diameters. Eres of SPBCL AuNPs increased with decreasing AuNP diameter down to \sim 70 nm, where E_{res} started to converge for smaller diameters to a value of \sim 2.3 eV. We accredit the observation that resonance energies and linewidths varied up to ~200 meV for some AuNP diameters to both the heterogeneity of the SPBCL AuNPs from 22 different arrays as well as the diameter being a simplified parameter describing the more complex actual AuNP shapes discussed above. Figure 3a also shows for comparison the resonances energies and linewidths of colloidal AuNSs with varying diameters, as indicated by the black stars and triangles, respectively. Apart from a small blueshift, which is likely caused by the above mentioned increased roundness of AuNSs, 55,56 the resonance energies agreed well between the SPBCL AuNPs and colloidal AuNSs, following the same trend of decreasing Eres with increasing diameter because of phase retardation. ⁶⁰ On the other hand, the linewidths were generally larger for the AuNSs, especially for diameters around 100 nm, where plasmon damping reached a minimum of ~300 meV for the SPBCL AuNPs.

The plasmonic damping in SPBCL AuNPs is dominated mostly by radiation damping with some contribution from electron-surface scattering. With the homogeneous single-particle linewidth and correlated structural information we isolated different contributions to plasmon damping of SPBCL AuNPs. A detailed understanding of different damping mechanisms is important for various applications, which typically seek reduced damping as longer plasmon lifetimes are generally advantageous.⁴⁵ The plasmon linewidth as a measure of damping in metal nanoparticles has been described as $\Gamma_{Total} = \Gamma_{Bulk} + \Gamma_{Total} = \Gamma_{To$ $\Gamma_{\text{Rad}} + \Gamma_{\text{Surf}} + \Gamma_{\text{CID}}$, comprising bulk damping Γ_{Bulk} , radiation damping Γ_{Rad} , electron-surface scattering Γ_{Surf} , and chemical interface damping Γ_{CID} . ^{44, 45} Assuming Γ_{CID} to be negligible (see Supporting Information that provides a detailed discussion of all damping contributions and their calculation), we suggest that the trends in plasmon damping of SPBCL AuNPs in Figure 3a can be attributed to increased Γ_{Rad} for large AuNPs above 100 nm in diameter and increased Γ_{Surf} as well as Γ_{Bulk} , for smaller AuNPs. To test this assignment, we computed Γ_{Rad} and Γ_{surf} using the individually determined volumes and thicknesses, as illustrated in Figure 3b for each SPBCL AuNP in blue and green, respectively. Because its scaling with the particle volume, Γ_{Rad} remained smaller than ~100 meV for AuNPs below 100 nm in diameter. Γ_{surf} started to rise significantly for diameters below ~60 nm. Considering that the respective AuNP thicknesses corresponded to at most half the diameter, this finding was in good agreement with the

electron mean free path of ~40 nm for Au,⁶¹ and in quite good agreement with reports of significant electron-surface scattering contributing to plasmon damping for nanorods with widths below 20 nm.⁴⁶ Subtracting the calculated Γ_{Rad} and Γ_{surf} from the measured linewidths yielded residual plasmon damping values (Figure 3c) that on average followed the frequency-dependent Γ_{Bulk} (binned black data points), increasing for larger resonance energies due to stronger interband transitions, as demonstrated by the gray shaded area. As already apparent from the magnitudes of the damping contributions given in Figure 3b, Figure S9 (top panel) illustrates that the linewidth was mainly broadened by Γ_{Rad} , although the smaller Γ_{surf} term was nevertheless needed to completely describe plasmon damping in these SPBCL AuNPs.

Despite the good agreement found for the decomposition of the measured single-particle linewidths of SPBCL AuNPs into the different plasmon damping contributions in Figure 3c, there was also a large spread in values for each resonance energy. The same was the case for the diameter as well (Figure 3a), which was chosen as the relevant size parameter to display because it was determined for every AuNP from SEM images. Thicknesses on the other hand were only inferred from AFM measurements of a subset of AuNPs (Figure 1d) and furthermore needed to be corrected to calculate more realistic values for V and Leff. (Figure S8). The uncertainty especially in AuNP thicknesses as well as approximating the in-plane dimensions of the different, mostly non-circular AuNP shapes by an average diameter ignored the actual AuNP shapes, leading to over- as well as under-estimation of size dependent damping contributions like Γ_{Rad} and Γ_{surf} . In particular, a simple scaling relationship between diameter and maximum thickness and the use of a single correction factor for an adjusted effective thickness (see Supporting information) were too simple to accurately account for the AuNP shape heterogeneity, but AFM measurements on ~1,400 SPBCL AuNPs was not feasible. Furthermore, experimental uncertainties in determining the AuNP diameters from a lower resolution environmental SEM, which had to be used because of the non-conductive nature of the glass substrate, could have further enhanced the spread in plasmon linewidths especially for the smaller SPBCL AuNPs. Lastly, while we assumed SPBCL AuNPs to be ligand-free, carbon residues of the decomposed polymer could have affected the surface scattering contribution. We therefore attribute the spread in resonance energies and linewidths collectively to these limitations. Similarly, note that the direct determination of A for Γ_{surf} following previous literature procedures was not successful as the data spread hindered this analysis. 44 Nevertheless, the almost quantitative agreement of our analysis with especially the binned data points (black line and error bars in Figure 3c) is actually quite remarkable.

The high quality plasmon resonances of SPBCL AuNPs imply a high degree of crystallinity. The absence of additional linewidth broadening that could not be accounted for by radiation damping and electron-surface damping is consistent with the high crystallinity shown above through Wulff construction theory and TEM analyses. The previously mentioned reduced plasmon damping in comparison to colloidal AuNSs of similar diameters makes even the larger plasmonic AuNPs prepared by SPBCL AuNPs attractive for potential applications. While high particle crystallinity likely contributed to their small plasmonic damping, the SPBCL AuNPs mainly profited from their smaller thicknesses compared to their base diameters and hence reduced volumes compared to AuNSs of equal diameter (Figure S10). The smaller volumes resulted in diminished radiation damping and hence smaller total damping considering that electron-surface scattering was found to play only a minor role, especially for SPBCL AuNPs with diameters larger than 60 nm. That the plasmon linewidth of the AuNSs was mainly dominated by radiation damping can be seen by the rise in plasmon damping as the AuNS diameter increased.

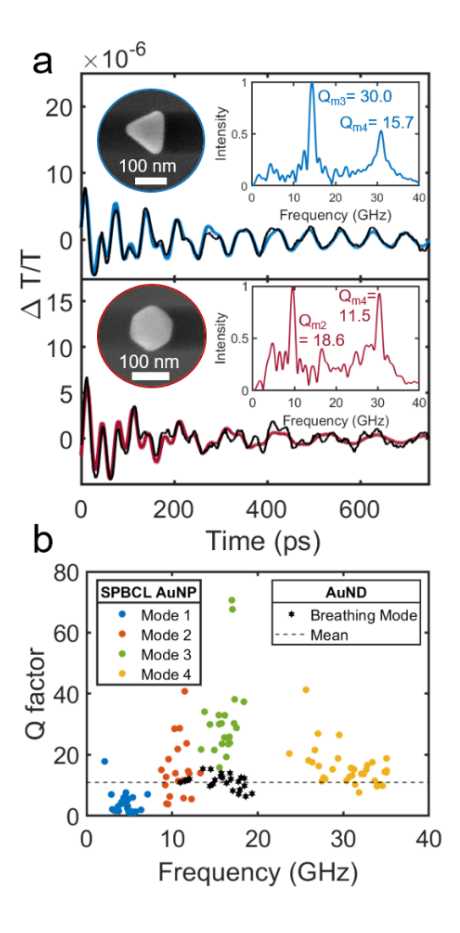


Figure 4. SPBCL-synthesized AuNPs supported several acoustic vibration modes with enhanced Q factors compared to AuNPs fabricated by electron beam lithography. (a) Representative transient transmission of a truncated triangular (top) and a hexagonal (bottom) AuNP, with convoluted acoustic

modes. The blue and red lines represent fits of damped cosine functions to the experimental data (black) to determine acoustic frequencies and Q factors. Note that only the oscillatory part of the transient transmission is displayed (see Figure S11 for the entire ultrafast response). Inset: FFT of the experimental data to isolate the main frequency components. For each illustrated AuNP two acoustic modes were identified, and the determined Q factors are shown next to the respective frequency component in the FFT. (b) Measured acoustic Q factors plotted against their frequency. From 55 truncated triangular, hexagonal, and circular AuNPs, we identified four modes based on differences in their acoustic frequencies. For comparison, acoustic Q factors for the in-plane breathing mode of EBL fabricated Au nanodisks (AuNDs) with diameters of 78 to 160 nm and hence comparable frequencies are displayed in black stars. The data for AuNDs was adapted from our previous work.⁴²

Because of their anisotropy, SPBCL AuNPs exhibit various acoustic modes. We characterized the mechanical properties of SPBCL AuNPs by evaluating their coherent acoustic breathing modes excited by ultrafast laser pulses in a single-particle pump-probe microscope. 400 nm pump pulses generated hot carriers that through electron-phonon coupling impulsively heated the lattice, launching acoustic vibrations that modulated the transmitted probe pulses at 800 nm as the plasmon is sensitive to the AuNP volume. Figure 4a displays example time-resolved transient transmission traces for a truncated triangular (blue) and a hexagonal (red) AuNP, ignoring the initial 30 ps response (Figure S11) and only focusing on the coherent oscillations. These oscillations were fit to a sum of damped cosine functions to extract acoustic frequencies v and damping times τ that together yield the Q factors, $Q = \pi v \tau$, following a previously reported methodology⁴³ that is summarized in the Supporting Information. We found that SPBCL AuNPs supported several acoustic modes between 0 and 40 GHz, likely due to their anisotropic structures. Despite the AuNP heterogeneity, we observed similarities in the acoustic modes of 55 measured AuNPs that had comparable maximum diameters between 125 and 150 nm and belonged to the first three shape categories. Based on the measured acoustic frequencies and Q factors, we identified 4 different modes with acoustic frequencies around 5 GHz, 10 GHz, 15 GHz, and 30 GHz. These modes repeatedly occurred throughout the set of measured AuNPs with varying intensities in the FFTs as shown in the insets of Figure 4a and Figure S12. While almost no AuNP exhibited all 4 modes, we assume that this observation was due to experimental challenges in identifying modes that were either weakly excited or did not sufficiently change the plasmon resonance to be detected.

SPBCL AuNPs are high quality acoustic oscillators. The acoustic Q factors of SPBCL AuNPs reached up to \sim 70, consistent with their high crystallinity. Figure 4b summaries the Q factors that were extracted from the analysis of the transient transmissions for 55 AuNPs. The average frequencies were identified as 4.4 ± 1.1 GHz, 10.7 ± 3.3 GHz, 16.1 ± 1.2 GHz, and 30.6 ± 3.2 GHz for modes 1 through 4,

respectively. The magnitudes of the Q factors depended strongly on the mode, with the smallest values of 4.2 ± 3.3 for mode 1, larger values of 15.3 ± 9.3 and 15 ± 6.2 for modes 2 and 4, and the largest values of 31.4 ± 13.2 for mode 3. Importantly, for mode 3 the Q factor reached a maximum of 70.6. These Q factors exceeded those previously reported for polycrystalline AuNPs, 14,20,62,63 and are comparable to those of crystalline colloidal AuNSs and Au nanorods. Specifically, in Figure 4b we also compare single-particle Q factors (mean value of 11.0 ± 2.5), previously determined for EBL fabricated AuNDs with diameters of 78 to 160 nm. The distribution of frequencies for each mode can be explained by the AuNP shape and size heterogeneity, while the distribution in Q was likely due to some variations in the crystallinity within the AuNPs (twin planes) and to differences in the particle-substrate contact quality. We also related each data point in Figure 4b to its corresponding AuNP shape (Figure S13) but found no clear trend in terms of larger Q values or preferred modes for specific AuNP shapes.

Depending on their frequency, the experimentally observed acoustic modes correspond to distinct displacement profiles. To understand the nature of the experimentally observed acoustic modes, we performed FEM simulations of a truncated triangular and a hexagonal AuNP with similar dimensions to the examples shown in Figure 4a to obtain spatially resolved displacement maps as illustrated in Figures 5a and 5b, respectively. Details of the FEM simulations are provided in the Supporting Information. Simulated displacement profiles visualize the vibrations and help identify sources of energy loss such as extrinsic damping into the environment or intrinsic damping in regions of defects. We identified 4 efficiently excited and detected acoustic modes at frequencies that reasonably matched with the experiment. We found that the displacement profiles of the 4 identified modes rapidly increased in complexity with increasing vibrational frequency, but also identified similarities between truncated triangular and hexagonal AuNPs. For example, the low-frequency mode 1 exhibited the overall largest and most-widespread displacement amplitudes for both shapes, albeit in predominantly the horizontal direction for the truncated triangular AuNP and uniformly directed for the hexagonal AuNP. In contrast, the modes with higher frequencies exhibited generally smaller displacement amplitudes with reduced magnitudes at specific locations.

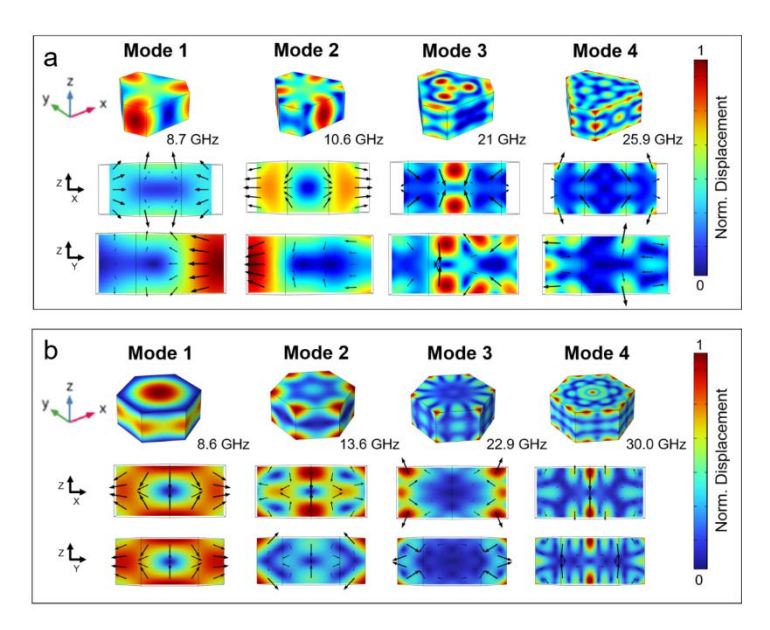


Figure 5. FEM simulations for identifying experimental modes and mode-specific damping sources.

a) Simulated displacement profiles of the truncated triangular AuNP based on FEM calculations, illustrating each mode profile. The top row offers a 3D perspective of the displacement across the AuNP, while the second and third rows correspond to the side views of tXZ and YZ cross sections through the AuNP center. The normalized displacements are color-coded with red being the largest displacement and dark blue indicating no displacement. b) Similar to a) for a hexagonal AuNP.

Acoustic mode engineering for SPBCL AuNPs has the potential to achieve consistently large Q factors that are desirable for applications in biosensing, ⁶⁹ sensitive mass spectrometry, ^{1,70} and optomechanical devices. ⁷¹ Assuming generally high crystallinity for substrate-supported SPBCL AuNPs and an air environment, the mode-dependent Q factor variations must be the result of distinct defects such as the twin plane in the AuNP center or acoustic damping into the substrate. In line with this hypothesis, mode 3 showed small displacements in the horizontal center plane of the truncated triangular AuNP as illustrated in Figure 5a, or at the bottom of the hexagonal AuNP as shown in Figure 5b. We suggest that these localizations of small displacement amplitudes at AuNP boundaries or defect sites such as the substrate interface and twin planes lead to reduced acoustic damping and hence larger Q factors for modes 2 through 4 compared to mode 1. This argument is supported by average Q factors around 30 for mode 3. We further suppose that the largest Q factors up to 70 were the result of especially crystalline AuNPs that were in particularly weak contact with the substrate and experienced both reduced intrinsic and extrinsic damping. Our findings indicate that it should be possible to design and fabricate highly efficient acoustic modes in crystalline SPBCL AuNPs through improvements in controlling their shape.

Conclusion

We studied the optical and mechanical properties of AuNPs that were fabricated by SPBCL and had diameters centered around 100 nm. We found that such SPBCL AuNPs could be produced with narrow diameter distributions but had heterogeneous morphologies that resembled different variations of a prismatic base-shape. The SPBCL AuNPs supported plasmon resonances that were comparable to those of nanospheres with similar diameters and offered improved plasmon damping. Both theoretical considerations based on Wulff construction theory as well as TEM images indicated that the SPBCL AuNPs were highly crystalline containing twin planes. High crystallinity was further confirmed by large acoustic Q factors.

Our work demonstrates the high-throughput and precise positioning of, for the first time, larger plasmonic nanoparticles on transparent substrates using SPBCL. With superior optical properties of these crystalline AuNPs and the ability to create large area arrays, the combination of SPBCL and the automated dark-field scattering acquisition developed here will allow for the detailed screening of nanoparticle sizes, shapes, and importantly multi-metallic compositions for desired electro-optical and opto-mechanic applications. Further optimization of the fabrication will undoubtedly improve on size and shape homogeneities of SPBCL plasmonic nanoparticles, although, on the other hand, intentionally creating gradients across the sample for different arrays coupled with high throughput optical characterization is also desired.

Associated Content

Supporting Information

Scanning probe block lithography; single-particle scattering spectroscopy; single-particle ultrafast transient transmission microscopy; Wulff construction; DDA simulations; FEM simulations; SEM; TEM; AFM; plasmonic damping calculations; Additional figures: AuNP shape distribution; AuNP size distribution; diameter dependence of the AuNP shape; discussion of side products; size and shape dependence of plasmon resonance energies; calculated electric fields from DDA simulations; TEM image of AuNP oxide layer; particle thickness correction; further analysis of plasmon damping; volume dependence of the plasmon resonance and damping; data analysis procedure of transient transmission traces; example traces and respective FFTs; shape dependence of the acoustic Q factor.

Author Information

Corresponding Author

Stephan Link - Department of Chemistry, Department of Electrical and Computer Engineering, and Smalley-Curl Institute, Rice University, Houston, Texas 77005, United States; orcid.org/00000002-4781-930X; Email: slink@rice.edu

Authors

Niklas Gross - Department of Chemistry, Rice University, Houston, Texas 77005, United States; orcid.org/0000-0002-2425-1029; Email: ng27@rice.edu

William Wang - Department of Chemistry, Rice University, Houston, Texas 77005, United States; Email: wlw6@rice.edu

Sadie Brasel - Department of Electrical and Computer Engineering, Rice University, Houston, Texas 77005, United States; orcid.org/0000-0002-2425-1029; Email: snb11@rice.edu

Emily K. Searles - Department of Chemistry, Rice University, Houston, Texas 77005, United States; orcid.org/0000-0002-2425-1029; Email: es54@rice.edu

Briley B. Bourgeois - Department of Materials Science & Engineering, Stanford University, Stanford, California 94305, United States; Email: bbourge6@stanford.edu

Jennifer D. Dionne - Department of Applied Physics, Stanford University, Stanford, California 94305, United States; Email: jdionne@stanford.edu

Christy F. Landes – Department of Chemistry, Department of Electrical and Computer Engineering, Department of Chemical and Biomolecular Engineering, and Smalley-Curl Institute, Rice University, Houston, Texas 77005, United States; orcid.org/0000-0003-4163-6497; Email: cflandes@rice.edu

Author Contributions

All authors have given approval to the final version of the manuscript.

Notes

The authors declare no competing financial interest.

Acknowledgements

This work was funded by the National Science Foundation, Center for Adopting Flaws as Features (NSF CHE-2124983). S.L. thanks the Robert A. Welch Foundation for support through the Charles W. Duncan, Jr.-Welch Chair in Chemistry (C-0002). C.F.L acknowledges funding from the Robert A. Welch Foundation (C-1787) and support through the Kenneth S. Pitzer-Schlumberger Chair in Chemistry. The

authors want to thank the Shared Equipment Authority at Rice University for providing instrumentation with which this work was in part conducted. The authors also want to thank Jared Magoline from TERAPRINT for his continuous support during the AuNP synthesis.

Abbreviations

SPBCL Scanning probe block-copolymer lithography

PPL Polymer-pen-lithography
EBL Electron beam lithography

Au Gold

PVP polyvinylpyrrolidone

SEM Scanning electron microscopy

AFM Atomic force microscopy

TEM Transmission electron microscopy

HRTEM High-resolution transmission electron microscopy

DDA Discrete dipole approximation

FEM Finite element method
AuNP Gold nanoparticle
AuNS Gold nanosphere
AuNDs Gold nanodisks

FFT Fast Fourier transform

Q factor Quality factor

CCD Charge-coupled device

References

- (1) Yu, K.; Sader, J. E.; Zijlstra, P.; Hong, M.; Xu, Q.-H.; Orrit, M. Probing silver deposition on single gold nanorods by their acoustic vibrations. *Nano Lett.* **2014**, *14*, 915-922.
- (2) Sprague-Klein, E. A.; Negru, B.; Madison, L. R.; Coste, S. C.; Rugg, B. K.; Felts, A. M.; McAnally, M. O.; Banik, M.; Apkarian, V. A.; Wasielewski, M. R.; et al. Photoinduced plasmon-driven chemistry in trans-1,2-bis(4-pyridyl)ethylene gold nanosphere oligomers. *Journal of the American Chemical Society* **2018**, *140*, 10583-10592.
- (3) Li, N.; Wu, F.; Han, Z. H.; Wang, X. F.; Liu, Y.; Yi, C. L.; Ye, S. S.; Lu, G. W.; Yu, L.; Nie, Z. H.; et al. Shape complementarity modulated self-assembly of nanoring and nanosphere hetero-nanostructures. *Journal of the American Chemical Society* **2020**, *142*, 11680-11684.
- (4) Barad, H. N.; Kwon, H.; Alarcon-Correa, M.; Fischer, P. Large area patterning of nanoparticles and nanostructures: Current status and future prospects. *ACS Nano* **2021**, *15*, 5861-5875.
- (5) Henzie, J.; Lee, M. H.; Odom, T. W. Multiscale patterning of plasmonic metamaterials. *Nat Nanotechnol* **2007**, *2*, 549-554.
- (6) O'Brien, K.; Lanzillotti-Kimura, N. D.; Rho, J.; Suchowski, H.; Yin, X. B.; Zhang, X. Ultrafast acousto-plasmonic control and sensing in complex nanostructures. *Nature Communications* **2014**, *5*, 4042.
- (7) Dhindsa, P.; Solti, D.; Jacobson, C. R.; Kuriakose, A.; Naidu, G. N.; Bayles, A.; Yuan, Y. G.; Nordlander, P.; Halas, N. J. Facet tunability of aluminum nanocrystals. *Nano Lett.* **2022**, *22*, 10088–10094.
- (8) Chen, Y. Q.; Bi, K. X.; Wang, Q. J.; Zheng, M. J.; Liu, Q.; Han, Y. X.; Yang, J. B.; Chang, S. L.; Zhang, G. H.; Duan, H. G. Rapid focused ion beam milling based fabrication of plasmonic nanoparticles and assemblies via "sketch and peel" strategy. *ACS Nano* **2016**, *10*, 11228-11236.
- (9) Kaneko, R.; Ichikawa, H.; Hosaka, M.; Sone, Y.; Imura, Y.; Wang, K. H.; Kawai, T. Hole, convex, and silver nanoparticle patterning on polystyrene nanosheets by colloidal photolithography at air-water interfaces. *Langmuir* **2022**, *38*, 8153-8159.
- (10) Baek, W.; Chang, H.; Bootharaju, M. S.; Kim, J. H.; Park, S.; Hyeon, T. Recent advances and prospects in colloidal nanomaterials. *Jacs Au* **2021**, *I*, 1849-1859.
- (11) Horak, M.; Bukvisova, K.; Svarc, V.; Jaskowiec, J.; Krapek, V.; Sikola, T. Comparative study of plasmonic antennas fabricated by electron beam and focused ion beam lithography. *Scientific Reports* **2018**, *8*, 9640
- (12) Lou, M. H.; Bao, J. L.; Zhou, L. A.; Naidu, G. N.; Robatjazi, H.; Bayles, A. I.; Everitt, H. O.; Nordlander, P.; Carter, E. A.; Halas, N. J. Direct h2s decomposition by plasmonic photocatalysis: Efficient remediation plus sustainable hydrogen production. *Acs Energy Letters* **2022**, *7*, 3666-3674.
- (13) Kawawaki, T.; Wang, H. B.; Kubo, T.; Saito, K.; Nakazaki, J.; Segawa, H.; Tatsuma, T. Efficiency enhancement of pbs quantum dot/zno nanowire bulk-heterojunction solar cells by plasmonic silver nanocubes. *ACS Nano* **2015**, *9*, 4165-4172.
- (14) Boggiano, H. D.; Berte, R.; Scarpettini, A. F.; Cortes, E.; Maier, S. A.; Bragas, A. V. Determination of nanoscale mechanical properties of polymers via plasmonic nanoantennas. *ACS Photonics* **2020**, *7*, 1403-1409.
- (15) Cai, R.; Xiang, H. D.; Yang, D.; Lin, K. T.; Wu, Y. Z.; Zhou, R. Y.; Gu, Z. J.; Yan, L.; Zhao, Y. L.; Tan, W. H. Plasmonic aupt@cus heterostructure with enhanced synergistic efficacy for radiophotothermal therapy. *Journal of the American Chemical Society* **2021**, *143*, 16113-16127.
- (16) Yu, S.; Jain, P. K. Plasmonic photosynthesis of c-1-c-3 hydrocarbons from carbon dioxide assisted by an ionic liquid. *Nature Communications* **2019**, *10*, 2022.
- (17) Xia, Y. N.; Xiong, Y. J.; Lim, B.; Skrabalak, S. E. Shape-controlled synthesis of metal nanocrystals: Simple chemistry meets complex physics? *Angewandte Chemie-International Edition* **2009**, *48*, 60-103. (18) Lin, H. X.; Lee, S. M.; Sun, L.; Spellings, M.; Engel, M.; Glotzer, S. C.; Mirkin, C. A. Clathrate colloidal crystals. *Science* **2017**, *355*, 931-935.

- (19) Della Picca, F.; Berte, R.; Rahmani, M.; Albella, P.; Bujjamer, J. M.; Poblet, M.; Cortes, E.; Maier, S. A.; Bragas, A. V. Tailored hypersound generation in single plasmonic nanoantennas. *Nano Lett.* **2016**, *16*, 1428-1434.
- (20) Medeghini, F.; Crut, A.; Gandolfi, M.; Rossella, F.; Maioli, P.; Vallee, F.; Banfi, F.; Del Fatti, N. Controlling the quality factor of a single acoustic nanoresonator by tuning its morphology. *Nano Lett.* **2018**, *18*, 5159-5166.
- (21) Tauzin, L. J.; Cai, Y. Y.; Smith, K. W.; Jebeli, S. A. H.; Bhattacharjee, U.; Chang, W. S.; Link, S. Exploring the relationship between plasmon damping and luminescence in lithographically prepared gold nanorods. *ACS Photonics* **2018**, *5*, 3541-3549.
- (22) Hulteen, J. C.; Vanduyne, R. P. Nanosphere lithography a materials general fabrication process for periodic particle array surfaces. *J Vac Sci Technol A* **1995**, *13*, 1553-1558.
- (23) Gao, H. W.; Henzie, J.; Odom, T. W. Direct evidence for surface plasmon-mediated enhanced light transmission through metallic nanohole arrays. *Nano Lett.* **2006**, *6*, 2104-2108.
- (24) Qin, D.; Xia, Y. N.; Whitesides, G. M. Soft lithography for micro- and nanoscale patterning. *Nat Protoc* **2010**, *5*, 491-502.
- (25) Lee, M. H.; Huntington, M. D.; Zhou, W.; Yang, J. C.; Odom, T. W. Programmable soft lithography: Solvent-assisted nanoscale embossing. *Nano Lett.* **2011**, *11*, 311-315.
- (26) Zhang, H. Y.; Liu, Y. W.; Ashokan, A.; Gao, C.; Dong, Y.; Kinnear, C.; Kirkwood, N.; Zaman, S.; Maasoumi, F.; James, T. D.; et al. A general method for direct assembly of single nanocrystals. *Advanced Optical Materials* **2022**, *10*, 2200179.
- (27) Vinnacombe-Willson, G. A.; Conti, Y.; Stefancu, A.; Weiss, P. S.; Cortes, E.; Scarabelli, L. Direct bottom-up in situ growth: A paradigm shift for studies in wet-chemical synthesis of gold nanoparticles. *Chem Rev* **2023**, *123*, 8488-8529.
- (28) Zhu, H.; Lussier, F.; Ducrot, C.; Bourque, M. J.; Spatz, J. P.; Cui, W. L.; Yu, L.; Peng, W.; Trudeau, L. E.; Bazuin, C. G.; et al. Block copolymer brush layer-templated gold nanoparticles on nanofibers for surface-enhanced raman scattering optophysiology. *Acs Appl Mater Inter* **2019**, *11*, 4373-4384.
- (29) Glass, R.; Moller, M.; Spatz, J. P. Block copolymer micelle nanolithography. *Nanotechnology* **2003**, *14*, 1153-1160.
- (30) Eichelsdoerfer, D. J.; Liao, X.; Cabezas, M. D.; Morris, W.; Radha, B.; Brown, K. A.; Giam, L. R.; Braunschweig, A. B.; Mirkin, C. A. Large-area molecular patterning with polymer pen lithography. *Nat Protoc* **2013**, *8*, 2548-2560.
- (31) Chai, J. A.; Huo, F. W.; Zheng, Z. J.; Giam, L. R.; Shim, W.; Mirkin, C. A. Scanning probe block copolymer lithography. *P Natl Acad Sci USA* **2010**, *107*, 20202-20206.
- (32) Brown, K. A.; Hedrick, J. L.; Eichelsdoerfer, D. J.; Mirkin, C. A. Nanocombinatorics with cantilever-free scanning probe arrays. *ACS Nano* **2019**, *13*, 8-17.
- (33) Chen, P. C.; Liu, X. L.; Hedrick, J. L.; Xie, Z.; Wang, S. Z.; Lin, Q. Y.; Hersam, M. C.; Dravid, V. P.; Mirkin, C. A. Polyelemental nanoparticle libraries. *Science* **2016**, *352*, 1565-1569.
- (34) Chen, P. C.; Liu, G. L.; Zhou, Y.; Brown, K. A.; Chernyak, N.; Hedrick, J. L.; He, S.; Xie, Z.; Lin, Q. Y.; Dravid, V. P.; et al. Tip-directed synthesis of multimetallic nanoparticles. *Journal of the American Chemical Society* **2015**, *137*, 9167-9173.
- (35) Kluender, E. J.; Hedrick, J. L.; Brown, K. A.; Rao, R.; Meckes, B.; Du, J. S. S.; Moreau, L. M.; Maruyama, B.; Mirkin, C. A. Catalyst discovery through megalibraries of nanomaterials. *P Natl Acad Sci USA* **2019**, *116*, 40-45.
- (36) Smith, P. T.; Ye, Z.; Pietryga, J.; Huang, J.; Wahl, C. B.; Hedlund Orbeck, J. K.; Mirkin, C. A. Molecular thin films enable the synthesis and screening of nanoparticle megalibraries containing millions of catalysts. *Journal of the American Chemical Society* **2023**, *145*, 14031-14043.
- (37) Liu, G. L.; Eichelsdoerfer, D. J.; Rasin, B.; Zhou, Y.; Brown, K. A.; Liao, X.; Mirkin, C. A. Delineating the pathways for the site-directed synthesis of individual nanoparticles on surfaces. *P Natl Acad Sci USA* **2013**, *110*, 887-891.

- (38) Shuang, B.; Chen, J. X.; Kisley, L.; Landes, C. F. Troika of single particle tracking programing: Snr enhancement, particle identification, and mapping. *Physical Chemistry Chemical Physics* **2014**, *16*, 624-634.
- (39) Boukouvala, C.; Ringe, E. Wulff-based approach to modeling the plasmonic response of single crystal, twinned, and core-shell nanoparticles. *J Phys Chem C* **2019**, *123*, 25501-25508.
- (40) Draine, B. T.; Flatau, P. J. Discrete-dipole approximation for periodic targets: Theory and tests. *J Opt Soc Am A* **2008**, *25*, 2693-2703.
- (41) Kessentini, S.; Barchiesi, D.; D'Andrea, C.; Toma, A.; Guillot, N.; Di Fabrizio, E.; Fazio, B.; Marago, O. M.; Gucciardi, P. G.; de la Chapelle, M. L. Gold dimer nanoantenna with slanted gap for tunable lspr and improved sers. *J Phys Chem C* **2014**, *118*, 3209-3219.
- (42) Gross, N.; Madadi, M.; Ostovar, B.; Dongare, P. D.; McCarthy, L. A.; Chiang, W. Y.; Chang, W. S.; Halas, N. J.; Landes, C. F.; Sader, J. E.; et al. Strong substrate binding modulates the acoustic quality factors in gold nanodisks. *J Phys Chem C* **2023**, *127*, 5054-5066.
- (43) Chang, W. S.; Wen, F. F.; Chakraborty, D.; Su, M. N.; Zhang, Y.; Shuang, B.; Nordlander, P.; Sader, J. E.; Halas, N. J.; Link, S. Tuning the acoustic frequency of a gold nanodisk through its adhesion layer. *Nature Communications* **2015**, *6*, 7022.
- (44) Foerster, B.; Joplin, A.; Kaefer, K.; Celiksoy, S.; Link, S.; Sonnichsen, C. Chemical interface damping depends on electrons reaching the surface. *ACS Nano* **2017**, *11*, 2886-2893.
- (45) Foerster, B.; Rutten, J.; Pham, H.; Link, S.; Sonnichsen, C. Particle plasmons as dipole antennas: State representation of relative observables. *J Phys Chem C* **2018**, *122*, 19116-19123.
- (46) Novo, C.; Gomez, D.; Perez-Juste, J.; Zhang, Z. Y.; Petrova, H.; Reismann, M.; Mulvaney, P.; Hartland, G. V. Contributions from radiation damping and surface scattering to the linewidth of the longitudinal plasmon band of gold nanorods: A single particle study. *Physical Chemistry Chemical Physics* **2006**, *8*, 3540-3546.
- (47) Cai, Y. Y.; Liu, J. G.; Tauzin, L. J.; Huang, D.; Sung, E.; Zhang, H.; Joplin, A.; Chang, W. S.; Nordlander, P.; Link, S. Photoluminescence of gold nanorods: Purcell effect enhanced emission from hot carriers. *ACS Nano* **2018**, *12*, 976-985.
- (48) Olmon, R. L.; Slovick, B.; Johnson, T. W.; Shelton, D.; Oh, S. H.; Boreman, G. D.; Raschke, M. B. Optical dielectric function of gold. *Phys. Rev. B* **2012**, *86*, 235147
- (49) Lee, S. A.; Ostovar, B.; Landes, C. F.; Link, S. Spectroscopic signatures of plasmon-induced charge transfer in gold nanorods. *J Chem Phys* **2022**, *156*, 064702.
- (50) Ashcroft, N. W.; Mermin, N. D. Solid state physics; Holt, Rinehart & Winston: New York, 1976.
- (51) Coronado, E. A.; Schatz, G. C. Surface plasmon broadening for arbitrary shape nanoparticles: A geometrical probability approach. *J Chem Phys* **2003**, *119*, 3926-3934.
- (52) Millstone, J. E.; Hurst, S. J.; Metraux, G. S.; Cutler, J. I.; Mirkin, C. A. Colloidal gold and silver triangular nanoprisms. *Small* **2009**, *5*, 646-664.
- (53) Piella, J.; Bastus, N. G.; Puntes, V. Size-controlled synthesis of sub-10-nanometer citrate-stabilized gold nanoparticles and related optical properties. *Chem Mater* **2016**, *28*, 1066-1075.
- (54) Kelly, K. L.; Coronado, E.; Zhao, L. L.; Schatz, G. C. The optical properties of metal nanoparticles: The influence of size, shape, and dielectric environment. *J Phys Chem B* **2003**, *107*, 668-677.
- (55) Shuford, K. L.; Ratner, M. A.; Schatz, G. C. Multipolar excitation in triangular nanoprisms. *J Chem Phys* **2005**, *123*, 114713
- (56) Grzeskiewicz, B.; Ptaszynski, K.; Kotkowiak, M. Near and far-field properties of nanoprisms with rounded edges. *Plasmonics* **2014**, *9*, 607-614.
- (57) nanoComposix. *Nanoxact gold nanospheres bare (citrate)*. 2023. Available at: https://nanocomposix.com/collections/product-line-nanoxact/products/nanoxact-gold-nanospheres-bare-citrate?variant=39660079382617. Accessed 2023 April 30.
- (58) Ringe, E.; Van Duyne, R. P.; Marks, L. D. Kinetic and thermodynamic modified wulff constructions for twinned nanoparticles. *J Phys Chem C* **2013**, *117*, 15859-15870.
- (59) Draine, B. T.; Flatau, P. J. Discrete-dipole approximation for scattering calculations. *J Opt Soc Am A* **1994**, *11*, 1491-1499.

- (60) Hartland, G. V. Optical studies of dynamics in noble metal nanostructures. *Chem Rev* **2011**, *111*, 3858-3887.
- (61) Gall, D. Electron mean free path in elemental metals. J Appl Phys 2016, 119, 085101
- (62) Kelf, T. A.; Tanaka, Y.; Matsuda, O.; Larsson, E. M.; Sutherland, D. S.; Wright, O. B. Ultrafast vibrations of gold nanorings. *Nano Lett.* **2011**, *11*, 3893-3898.
- (63) Yi, C. Y.; Su, M. N.; Dongare, P. D.; Chakraborty, D.; Cai, Y. Y.; Marolf, D. M.; Kress, R. N.; Ostovar, B.; Tauzin, L. J.; Wen, F. F.; et al. Polycrystallinity of lithographically fabricated plasmonic nanostructures dominates their acoustic vibrational damping. *Nano Lett.* **2018**, *18*, 3494-3501.
- (64) Yu, K.; Zijlstra, P.; Sader, J. E.; Xu, Q. H.; Orrit, M. Damping of acoustic vibrations of immobilized single gold nanorods in different environments. *Nano Lett.* **2013**, *13*, 2710-2716.
- (65) Ruijgrok, P. V.; Zijlstra, P.; Tchebotareva, A. L.; Orrit, M. Damping of acoustic vibrations of single gold nanoparticles optically trapped in water. *Nano Lett.* **2012**, *12*, 1063-1069.
- (66) Cardinal, M. F.; Mongin, D.; Crut, A.; Maioli, P.; Rodriguez-Gonzalez, B.; Perez-Juste, J.; Liz-Marzan, L. M.; Del Fatti, N.; Vallee, F. Acoustic vibrations in bimetallic au@pd core-shell nanorods. *Journal of Physical Chemistry Letters* **2012**, *3*, 613-619.
- (67) Ostovar, B.; Su, M.-N.; Renard, D.; Clark, B. D.; Dongare, P. D.; Dutta, C.; Gross, N.; Sader, J. E.; Landes, C. F.; Chang, W.-S.; et al. Acoustic vibrations of al nanocrystals: Size, shape, and crystallinity revealed by single-particle transient extinction spectroscopy. *The Journal of Physical Chemistry A* **2020**, *124*, 3924-3934.
- (68) Major, T. A.; Crut, A.; Gao, B.; Lo, S. S.; Del Fatti, N.; Vallee, F.; Hartland, G. V. Damping of the acoustic vibrations of a suspended gold nanowire in air and water environments. *Physical Chemistry Chemical Physics* **2013**, *15*, 4169-4176.
- (69) Arlett, J. L.; Myers, E. B.; Roukes, M. L. Comparative advantages of mechanical biosensors. *Nat Nanotechnol* **2011**, *6*, 203-215.
- (70) Devkota, T.; Yu, K.; Hartland, G. V. Mass loading effects in the acoustic vibrations of gold nanoplates. *Nanoscale* **2019**, *11*, 16208-16213.
- (71) Lin, K. H.; Lai, C. M.; Pan, C. C.; Chyi, J. I.; Shi, J. W.; Sun, S. Z.; Chang, C. F.; Sun, C. K. Spatial manipulation of nanoacoustic waves with nanoscale spot sizes. *Nat Nanotechnol* **2007**, *2*, 704-708.